

Supporting Information for

Rapid and efficient removal of Cr(VI) by core-shell magnetic mesoporous polydopamine nanocomposite: Roles of mesoporous structure and redox-active functional groups

Qian Yang ^a, Huilin Wang ^a, Fangbai Li ^b, Zhi Dang ^c, Lijuan Zhang ^{a,*}

^a Guangdong Provincial Key Lab of Green Chemical Product Technology, School of Chemistry and Chemical Engineering, South China University of Technology, Guangzhou 510640, P R China. E-mail: celjzh@scut.edu.cn. Telephone/Fax: +86-20-87112046.

^b National-Regional Joint Engineering Research Center for Soil Pollution Control and Remediation in South China, Guangdong Key Laboratory of Integrated Agro-environmental Pollution Control and Management, Institute of Eco-environmental and Soil Sciences, Guangdong Academy of Sciences, Guangzhou 510650, China.

^c Key Lab of Pollution Control and Ecosystem Restoration in Industry Cluster, Ministry of Education, School of Environment and Energy, South China University of Technology, Guangzhou 510006, P R China.

1.1 Synthesis of mesoPDA and Fe₃O₄@PDA

To explore the influences of micro-mesoscopic and compositions structures of Fe₃O₄@mesoPDA on its adsorption performance, two other PDA-based adsorbents (mesoPDA, Fe₃O₄@PDA) were also prepared. The synthesis process of mesoporous polydopamine nanosphere (named as mesoPDA) was similar to that of Fe₃O₄@mesoPDA except without the addition of Fe₃O₄, and the synthesis process of magnetic polydopamine (named as Fe₃O₄@PDA) was also similar to that of Fe₃O₄@mesoPDA without the addition of templating agent F127 and pore-enlarging agent TMB.

1.2 Characterizations

Fourier infrared (FT-IR) (Vector 33-IR, Bruker) was tested to analyze the functional group composition of adsorbent before and after adsorption. Qualitative and semi-quantitative analysis of adsorbent functional group before and after adsorption was characterized by X-ray photoelectron spectroscopy (XPS, K-Alpha, Thermo Fisher Scientific), and its spectra were analyzed with XPSPEAK 41 software. The dynamic light scattering (DLS, Malvern Zetasizer Nano S) was employed to determine the Zeta potential of the sample surface under different pH values. X-ray diffraction spectroscopy (XRD) was recorded on a Bruker D8 Advance diffractometer equipped with Cu K α radiation (45 kV, 40 mA). The surface microstructure and morphology of the adsorbent were observed using the field scanning electron microscope (FESEM, SU8220) and transmission electron microscope (TEM, JEOL JEM-2100). The nitrogen adsorption-desorption isotherm was obtained from the ASAP 2020 analyzer (Micromeritics) at 77K. All of the samples were degassed under vacuum at 100°C for 12 h before the measurement. The Brunauer-Emmett-Teller (BET) method was utilized to calculate the specific surface area with P/P_0 in the range of 0.05-0.5. The corresponding size distribution curve and the total pore volume were obtained by the Barrett-Joyner-Halenda (BJH) model from the desorption branches of the isotherms. Thermogravimetric analysis (TGA) was conducted on a TG 209F3 thermal analyzer

from room temperature to 700°C with a heating rate of 10 °C/min under a nitrogen atmosphere. The magnetic property of the sample was measured by vibrating sample magnetometer (VSM-SQUID, Quantum Design) under a magnetic field from -20000 to 20000 Oe at room temperature.

1.3 Adsorption cycle and regeneration

Through adsorption-desorption experiments, the regeneration and reusability of Fe₃O₄@mesoPDA were evaluated. Firstly, 1 g/L Fe₃O₄@mesoPDA was added to 150 mL of Cr(VI) solution (200 ppm, pH=1.5) and adsorbed for 2 h at 298 K. And then the solid and solution were magnetically separated, and analyzed the residual Cr(VI) concentration in the filtrate. After that, 150 mL NaOH solution (1 M) was used to desorb the Cr(VI)-loaded Fe₃O₄@mesoPDA for 2 h. To further regenerate the active sites, the adsorbent after desorption was recovered by the addition of 100 mL of HCl solution (0.01 M) and shaking for 1.0 h. Subsequently, the adsorbent was magnetically enriched, washed thoroughly with ultrapure water, and dried. The regenerative adsorbent was reused in the next adsorption cycle under the same adsorption conditions, and the regeneration performance of Fe₃O₄@mesoPDA was estimated by the Cr(VI) removal efficiency after every adsorption-regeneration cycles.

1.4 Adsorption kinetics

The pseudo-first-order model, pseudo-second-order model, and intra-particle diffusion model were employed to evaluate the kinetic data of Cr(VI) on PDA-based adsorbents, and their linearized equations are expressed in Eqs. (1)~(3), respectively.

$$\ln (q_e - q_t) = \ln q_e - k_1 t \quad (1)$$

$$\frac{t}{q_t} = \frac{1}{k_2 q_e^2} + \frac{1}{q_e} t \quad (2)$$

$$q_t = Kt^{1/2} + C \quad (3)$$

Where q_e and q_t are the adsorption capacity (mg/g) at equilibrium and at time t (min); k_1 (min^{-1}), k_2 ($\text{g}/\text{mg}\cdot\text{min}$), and K ($\text{mg}/\text{g}\cdot\text{min}^{1/2}$) represent the adsorption rate constants for the pseudo-first-order model, pseudo-second-order model, and intra-particle diffusion model, respectively; C is a constant related to the thickness of the boundary layer.

1.5 Adsorption isotherms

Adsorption isotherms of Cr(VI) on PDA-based adsorbents were described by Langmuir, Freundlich, and D-R adsorption isotherm models.

Langmuir adsorption isotherm is a monolayer adsorption model, and the linearized model is expressed as follow:

$$\frac{C_e}{q_e} = \frac{1}{bq_m} + \frac{C_e}{q_m} \quad (4)$$

Where q_e and q_m are the equilibrium adsorption capacity (mg/g) and the maximum adsorption capacity (mg/g), respectively; C_e is the equilibrium concentration (mg/L); b represents for the equilibrium adsorption constant (L/mg).

The dimensionless separation factor R_L is a basic characteristic of the Langmuir model and is represented by Eq. (5).

$$R_L = \frac{1}{1 + bC_0} \quad (5)$$

R_L could be used to determine the favorability of an adsorption process. According to the value of R_L , the adsorption process could be divided into four probabilities: irreversible adsorption ($R_L=0$), favorable adsorption ($0 < R_L < 1$), linear adsorption ($R_L=1$), and unfavorable adsorption ($R_L > 1$).

Freundlich adsorption isotherm is suitable for multilayer adsorption on a heterogeneous adsorbent surface, and the linearized model is expressed as follow:

$$\ln q_e = \frac{1}{n} \ln C_e + \ln K_F \quad (6)$$

Where K_F is a Freundlich constant and represents the adsorption capacity of adsorbent; n is the heterogeneity factor related to the adsorption performance of adsorbent, and

$n > 1$ is the preferential adsorption whereas $n < 1$ for multi-layer adsorption.

The D-R isotherm model can be used to distinguish between physical adsorption and chemical adsorption, and its linear expression is:

$$\ln q_e' = \ln q_m' - K' \varepsilon^2 \quad (7)$$

Where q_e' and q_m' are respectively the equilibrium adsorption capacity (mol/g) and the maximum adsorption capacity (mol/g); K' is a constant related with adsorption energy (mol^2/kJ^2); ε is the Polanyi potential, and is equal to $RT \ln(1 + 1/C_e)$; C_e is the equilibrium concentration (mol/L); R is the gas constant ($8.314 \times 10^{-3} \text{ kJ/K}\cdot\text{mol}$); T is the absolute temperature (K).

The mean free energy of adsorption (E , kJ/mol) from K' of D-R isotherm is:

$$E = \frac{1}{\sqrt{2K'}} \quad (8)$$

1.6 Adsorption thermodynamics

The adsorption thermodynamic parameters including Gibb's free energy change (ΔG^0 , kJ/mol), enthalpy change (ΔH^0 , kJ/mol), and entropy change (ΔS^0 , kJ/mol·K) were calculated according to the following equation:

$$K_D = \frac{1000q_e}{C_e} \quad (9)$$

$$\Delta G^0 = -RT \ln K_D^0 \quad (10)$$

$$\ln K_D^0 = \frac{\Delta S^0}{R} - \frac{\Delta H^0}{RT} \quad (11)$$

Where K_D (mL/g) is the partition coefficient, and $\ln K_D^0$ is calculated from the intercept of plot of $\ln K_D$ versus C_e ; T (K) is the reaction temperature and R is the gas constant ($8.314 \text{ J/mol}\cdot\text{K}$); ΔH^0 and ΔS^0 were obtained from the slope and intercept of plot of K_D^0 versus $1/T$.

1.7 Effects of coexisting ions

Considering that cations and anions usually coexist in the natural environment and may

compete with Cr(VI) for the adsorption sites, the effects of ubiquitous cations and anions (i.e. Na⁺, K⁺, Ca²⁺, Cl⁻, NO³⁻, SO₄²⁻, PO₄³⁻) on the Cr(VI) removal were evaluated, and the result is shown in **Fig. S8**. It could be seen clearly that Fe₃O₄@mesoPDA had excellent selectivity for Cr(VI) in the presence of other coexisting ions with different concentrations. This may be mainly related to the properties and adsorption mechanisms of the adsorbent. Under strong acid conditions, there was strong electrostatic repulsion between coexisting cations and protonation adsorbent surface, so the coexisting cations had a negligible influence on the removal of anionic Cr(VI). As for coexisting anions including Cl⁻, NO³⁻, SO₄²⁻, PO₄³⁻, it was expected that they could theoretically compete with anionic Cr(VI) for the positive charge adsorption sites on the surface of Fe₃O₄@mesoPDA. However, the adsorption of Cr(VI) onto Fe₃O₄@mesoPDA was dominated by chemical reduction, and the Cr(VI) (HCrO₄⁻) adsorbed on the surface of the adsorbent was quickly reduce to Cr(III) by the electron-rich PDA shell layers. According to the principle of Le Chatelier, the adsorption equilibrium moved forward, which was beneficial to further promote the adsorption and reduction of Cr(VI) [1]. Moreover, compared with Cr(VI) (HCrO₄⁻), the coexisting anions were weaker oxidability [2], so they had little effect on the Cr(VI) adsorption performance of Fe₃O₄@mesoPDA.

1.8 Regeneration performance of Fe₃O₄@mesoPDA

The recycling regeneration performance is also an important index to evaluate the practical application adsorbent, which is of great significance to cut the use cost of the adsorbent. In this work, the cyclic regeneration performances of Fe₃O₄@mesoPDA were studied with 1 M NaOH solution as the desorption agent *via* five consecutive cycles of adsorption-desorption experiments. As shown in **Fig. S9A**, Fe₃O₄@mesoPDA maintain its efficient and rapid adsorption capacity for Cr(VI) in the first three cycles.

With the increase of the number of cycles, the removal efficiency of Cr(VI) dropped rapidly, and the removal efficiency of the fifth cycle was only 35.65%. The main reasons for the rapid decline of adsorption capacity were that the Cr(VI) adsorption mechanism of Fe₃O₄@mesoPDA was mainly redox reaction, and the physicochemical properties of adsorbent were irreversibly changed after multiple cycles including the decrease of specific surface area and pore size, and reductive functional groups, this changes of which were also further supported from the SEM image of Fe₃O₄@mesoPDA after 5 adsorption cycles (**Fig. S9B**).

1.9 Analysis of adsorption thermodynamic

As shown in **Fig. S5** and **Table S5**, the Cr(VI) adsorption onto Fe₃O₄@PDA and mesoPDA fit better by the Langmuir model, indicating the adsorption of Cr(VI) on the above two adsorbents is monolayer adsorption. The separation constants (R_L) of Fe₃O₄@PDA and mesoPDA were in the range of 0~1 at three different temperatures, suggesting the Cr(VI) adsorption was favorable adsorption. The maximum adsorption capacity of Fe₃O₄@PDA and mesoPDA were respectively 833.33~952.38 and 442.48~92.61 mg/g in pH=1.5. From **Fig. S5E** and **Table S7**, the experimental data of Fe₃O₄@PDA and mesoPDA fit well with the D-R isotherm model, and their mean adsorption energy values were both greater than 16 kJ/mol, suggesting the Cr(VI) adsorption on Fe₃O₄@PDA and mesoPDA were mainly chemical adsorption. This conclusion was also consistent with the analysis of their kinetic models.

The adsorption thermodynamic behaviors of Fe₃O₄@PDA, mesoPDA, and Fe₃O₄@mesoPDA have been studied *via* different thermodynamic parameters such as adsorption free energy (ΔG^0), adsorption enthalpy (ΔH^0), adsorption entropy (ΔS^0), and the related parameters are calculated from the slope and intercept of the plot of $\ln K_D$ versus $1/T$ (**Fig. S10**), and displayed in **Table S7**. All the relevant calculation formulas were calculated according to the Eqs. (9)~(11). In the temperature range of 298~318 K,

the adsorption free energies (ΔG^0) were negative, and decreased with the increase in temperature, indicating that the Cr(VI) adsorption processes on above three adsorbents were the spontaneous processes and the spontaneity increased with temperature. Moreover, the positive values of adsorption enthalpy (ΔH^0) indicated that the adsorption processes were endothermic, which were also confirmed by the increase of K_F , q_{max} , b values from adsorption isotherm models with the increase of temperature. Further, the positive value of adsorption entropy (ΔS^0) indicated that the randomness of the solid-liquid interface increased during the adsorption process. Among the three adsorbents, the ΔG^0 value of mesoPDA was the smallest, and the ΔH^0 and ΔS^0 values of mesoPDA were both the largest, demonstrating a stronger Cr(VI) adsorption affinity on mesoPDA owing to its biggest specific surface area and more active adsorption functional groups [3].

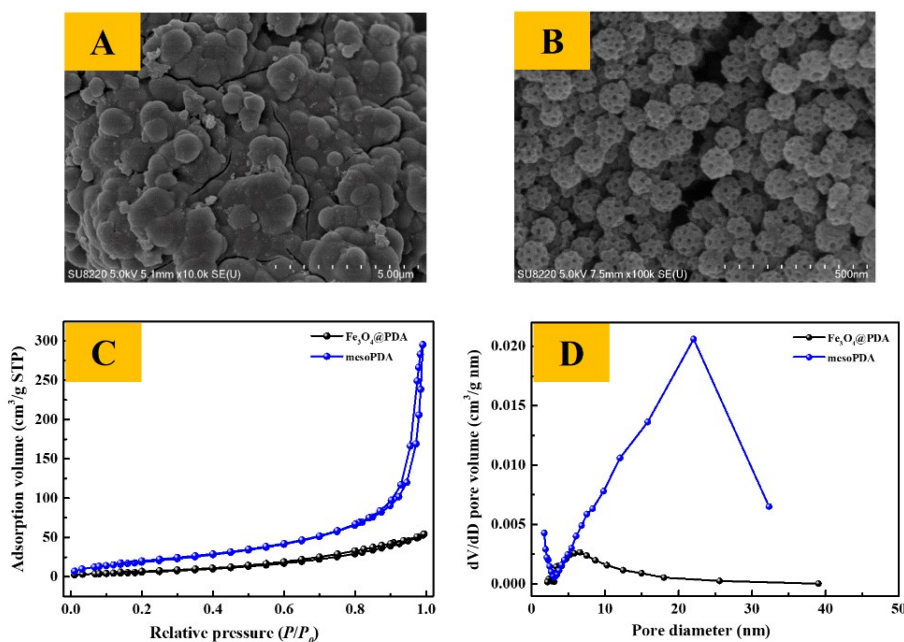


Fig. S1 SEM images of Fe₃O₄@PDA (A) and mesoPDA (B); nitrogen adsorption-desorption isotherms (C) and pore size distributions (D) of Fe₃O₄@PDA and mesoPDA.

Due to lack of the dispersion of the template, Fe₃O₄@PDA was composed of uneven size microspheres and glued together into a block structure (**Fig. S1A**). With the help of F127 and TMB, mesoPDA presented a uniform spherical morphology with a diameter of 93.4 ± 4.9 nm and a clear mesoporous structure on the surface (**Fig. S1B**). Contrastingly, mesoPDA showed smaller particle size, mesopore size, and worse uniformity of mesopore channel than Fe₃O₄@mesoPDA. The reason for this phenomenon may be that the self-polymerization of dopamine composite micelles has less resistance than the surface growth of nanoparticles [4], thus the growth rate of composite micelles is faster to form larger particle size. Additionally, TMB as a pore-enlarging agent could not only bind tightly to the hydrophobic blocks PPO of F127, but also has a high affinity with PDA oligomers through π - π stacking [5]. The partial PDA oligomers are attached to the surface of Fe₃O₄ with metal-chelating interaction in the synthesis of Fe₃O₄@mesoPDA, which may also affect the uniformity and pore size of the mesopore structure. As shown in **Fig. S1C** and **D**, Fe₃O₄@PDA has the type-III isotherm, and mesoPDA has the typical type-IV isotherm with a distinct H3 hysteresis

loop, and its average pore size is 20.4 nm. Fe₃O₄@PDA still exhibited a certain specific surface area and pore volume deriving from the stacking of dopamine oligomers. However, the specific surface area and pore volume of mesoPDA dramatically increased with the aid of F127 and TMB (**Table S1**).

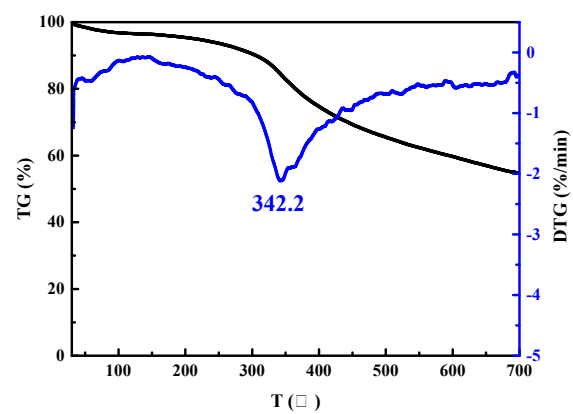


Fig. S2 TGA curve of mesoPDA.

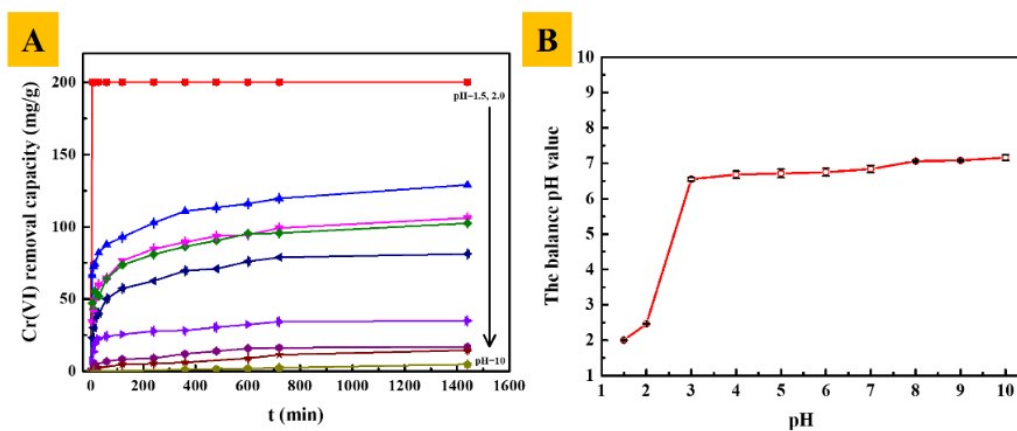


Fig. S3 Effects of the initial pH values from 1.5 to 10 along with adsorption time (A) and the pH value change (B) on the removal of Cr(VI). (Conditions: $C_0(\text{VI})=200$ ppm, adsorbent dose =1g/L, $T=298\text{K}$)

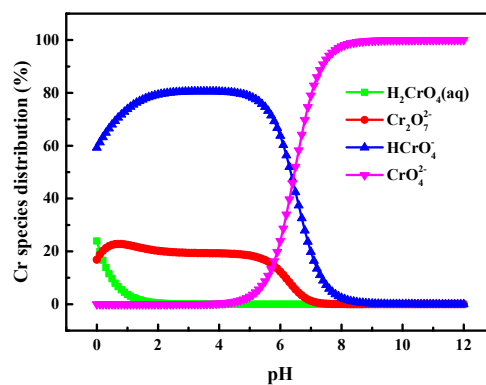


Fig. S4 Cr(VI) species distribution calculated by a chemical speciation model (Visual MINTEQ version 3.0). (Condition: $C_0(\text{VI})=200$ ppm)

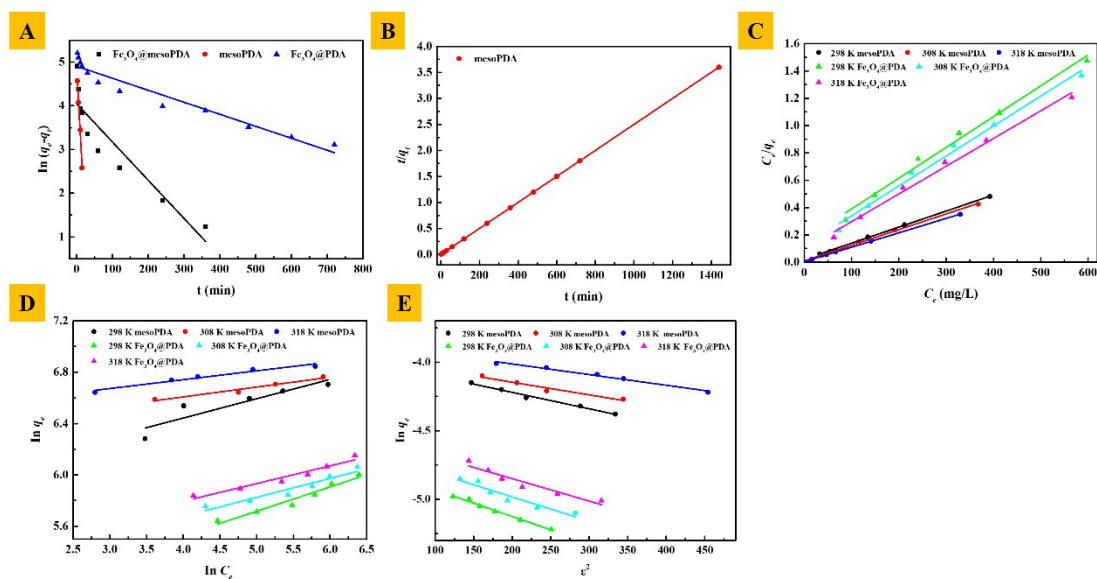


Fig. S5 Linear pseudo-first-order adsorption model plot (A) and linear pseudo-second-order adsorption model plot (B) for kinetic data (Conditions: $C_0(\text{VI})=200$ ppm, adsorbent dose = 0.5 g/L, pH=1.5, $T=298$ K); Langmuir isotherm plot (C), Freundlich isotherm plot (D), and D-R isotherms (E) for the adsorption of Cr(VI) at different temperatures (Conditions: $C_0(\text{VI})=200$ ppm, adsorbent dose = 0.5 g/L, pH=1.5) .

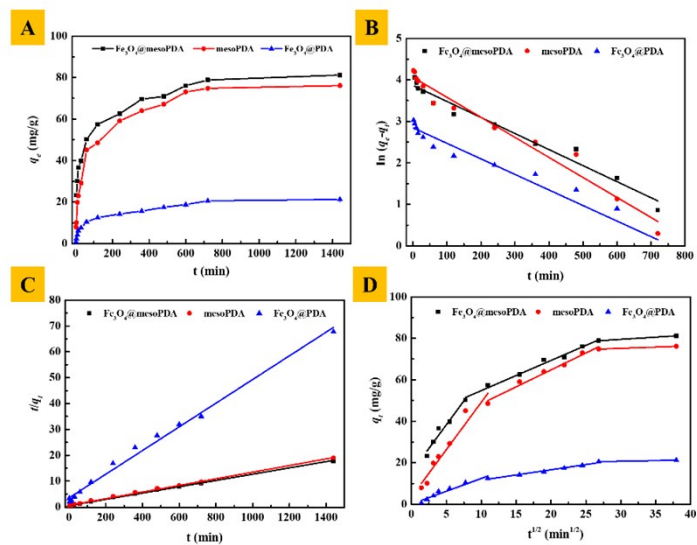


Fig. S6 Kinetics of Cr(VI) adsorption (A), linear pseudo-first-order adsorption model plot (B) and linear pseudo-second-order adsorption model plot (C) for kinetic data, intraparticle diffusion models (D) for adsorption of Cr(VI). (Condition: $C_0(\text{VI})=200$ ppm, adsorbent dose = 1.0 g/L, pH=6.0, $T=298$ K)

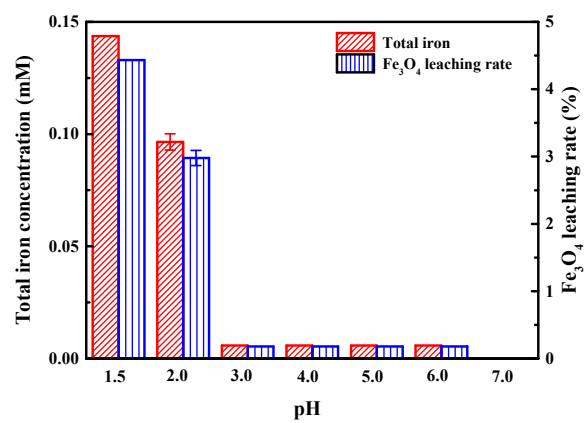


Fig. S7 The leaching rate of Fe₃O₄ under different pH values.

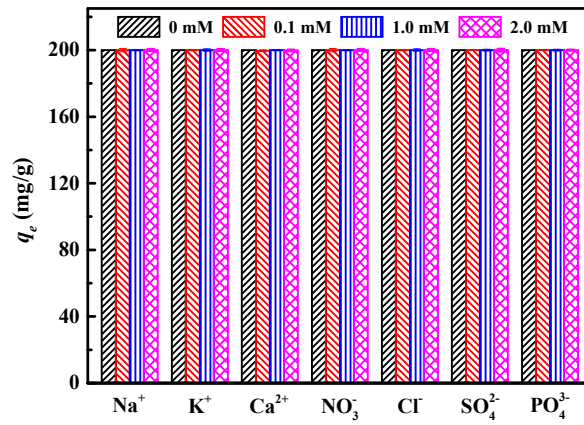


Fig. S8 Effects of coexisting ions on the Cr(VI) removal. (Conditions: $C_0(\text{VI})=200$ ppm, adsorbent dose =1.0 g/L, pH=1.5, $T=298$ K, adsorption time: 2 h)

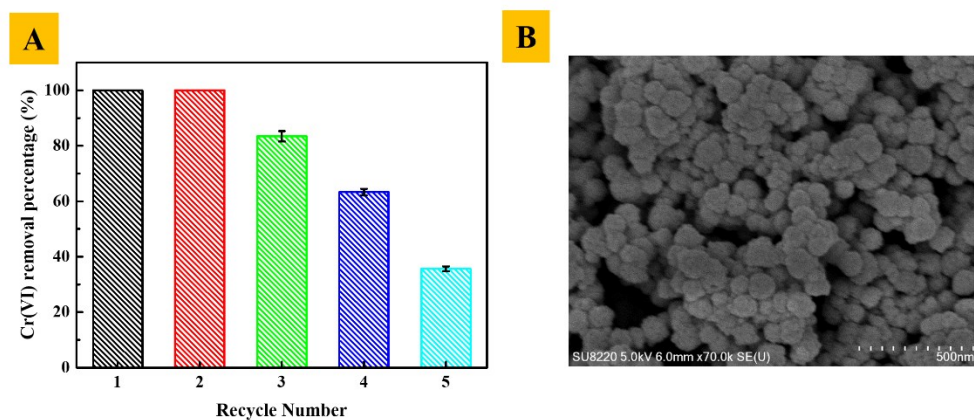


Fig. S9 Recycle adsorption performance of Fe₃O₄@mesoPDA (A) and SEM image of Fe₃O₄@mesoPDA after five times of Cr(VI) adsorption (B). (Conditions: $C_0(\text{VI})=200$ ppm, adsorbent dose =1.0 g/L, pH=1.5, $T=298$ K, adsorption time: 2 h)

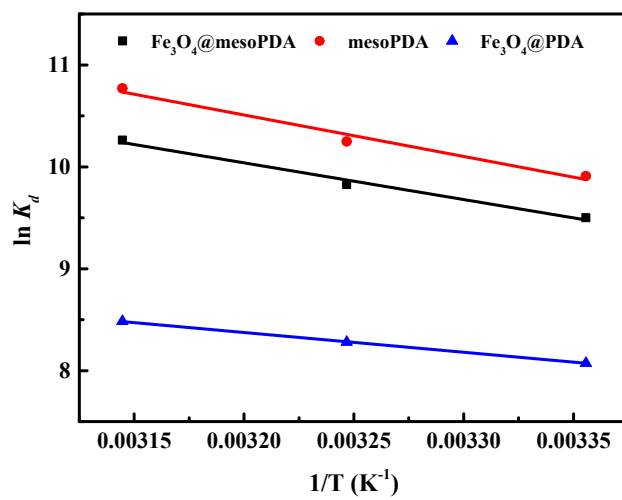


Fig. S10 Linear plot of $\ln K_D$ versus $1/T$ (F).

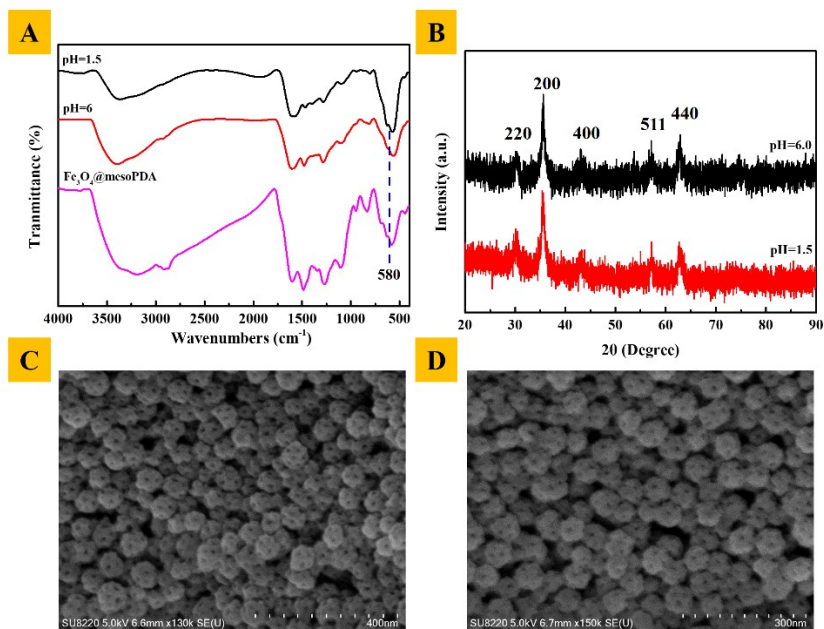


Fig. S11 FT-IR (A) and XRD (B) of $\text{Fe}_3\text{O}_4@\text{mesoPDA}$ after Cr(VI) adsorption under pH=1.5 and 6.0; SEM images of $\text{Fe}_3\text{O}_4@\text{mesoPDA}$ after Cr(VI) adsorption under pH=1.5 (C) and 6.0 (D).

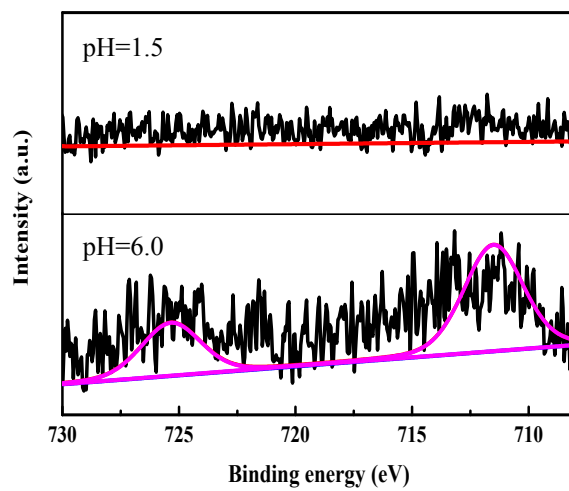


Fig. S12 XPS Fe 2p spectra of $\text{Fe}_3\text{O}_4@\text{mesoPDA}$ after Cr(VI) adsorption in pH=1.5 and 6.0.

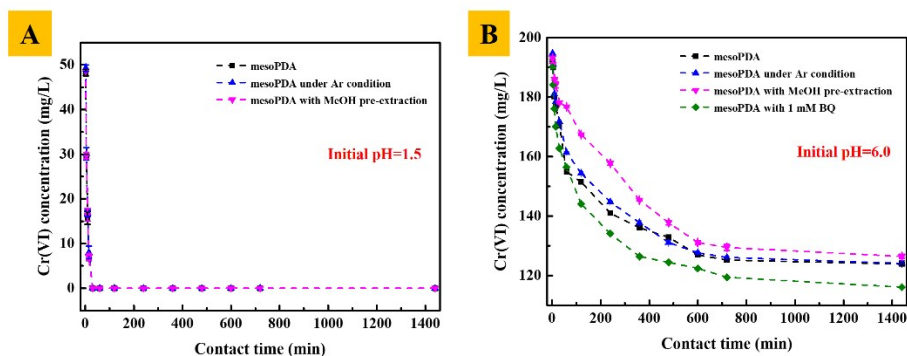


Fig. S13 The quenching effects of different scavengers on Cr(VI) removal kinetics by mesoPDA at pH=1.5 (A) (Conditions: $C_0(\text{VI})=200$ ppm, adsorbent dose=0.5 g/L, $T=298$ K) and pH=6.0 (B) (Conditions: $C_0(\text{VI})=200$ ppm, adsorbent dose=1.0 g/L, $T=298$ K).

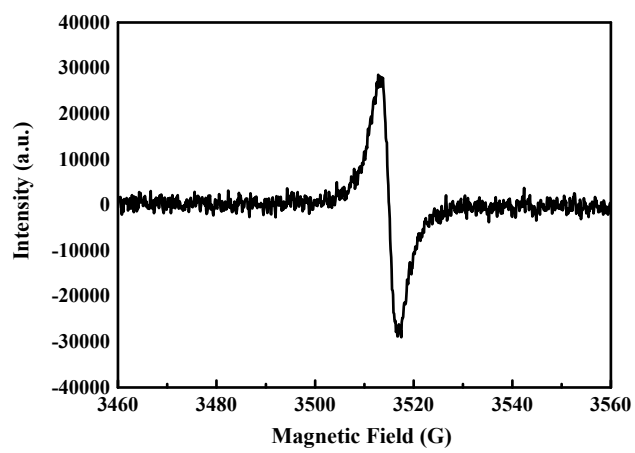


Fig. S14 EPR spectrum of Fe₃O₄@mesoPDA.

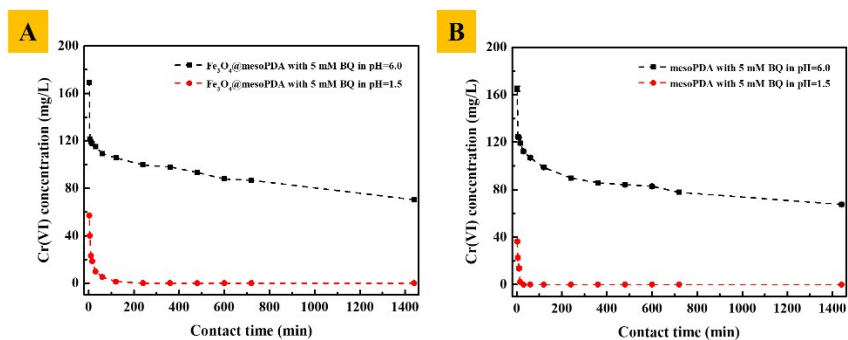


Fig. S15 Kinetics of Cr(VI) adsorption on $\text{Fe}_3\text{O}_4@mesoPDA$ (A) and mesoPDA (B) with 5 mM 1,4-benzoquinone in the pH=1.5 and 6.0. (Conditions: $C_0(\text{VI})=200$ ppm, $T=298$ K)

Table S1 Physicochemical properties of the different samples

Samples	BET surface (m ² /g)	Pore volume (cm ³ /g)	Pore size (nm)
Fe ₃ O ₄ @PDA	25.48	0.082	/
mesoPDA	75.60	0.446	20.4
Fe ₃ O ₄ @mesoPDA	63.54	0.374	18.76

Table S2 Surface elemental composition and relation content of functional groups in $\text{Fe}_3\text{O}_4@\text{mesoPDA}$ before and after Cr(VI) adsorption in $\text{pH}=1.5$ and $\text{pH}=6.0$.

Sample	XPS (At %)					Relation content of Functional groups (%)							
	C	O	N	Fe	Cr	C-O	C=O	Cr-O	-NH-	=N-	-NH ₂	Cr(III)	Cr(VI)
$\text{Fe}_3\text{O}_4@\text{mesoPDA}$	69.36	23.10	7.15	0.39	/	62.39	37.61	/	51.47	22.74	25.79	/	/
Adsorption in $\text{pH}=1.5$	55.63	34.24	5.20	0.47	4.47	32.07	56.43	11.50	39.76	40.68	19.55	81.77	18.23
Adsorption in $\text{pH}=6.0$	54.86	35.96	4.59	0.52	4.07	35.84	53.30	10.86	39.06	41.72	19.22	64.73	35.27

Table S3 Kinetic parameters of Cr(VI) adsorption onto Fe₃O₄@mesoPDA, mesoPDA, Fe₃O₄@PDA in pH=1.5.

	C_0 (mg/L)	$q_e(\text{exp})$ (mg/g)	Pseudo-first-order model			Pseudo-second-order model		
			k_1 (min ⁻¹)	$q_e(\text{cal})$ (mg/g)	R^2	k_2 (g/mg·min)	$q_e(\text{cal})$ (mg/g)	R^2
Fe ₃ O ₄ @mesoPDA	200	400	8.75×10^{-3}	81.83	0.830	1.079×10^{-3}	400	0.999
mesoPDA	200	400	0.14964	129.69	0.993	7.13×10^{-3}	400	1
Fe ₃ O ₄ @PDA	200	26781	2.75×10^{-3}	134.84	0.932	1.115×10^{-4}	265.25	0.995

	Intraparticle diffusion model								
	C_1	K_1	R_1^2	C_2	K_2	R_2^2	C_3	K_3	R_3^2
	(g/mg·min ^{1/2})			(g/mg·min ^{1/2})			(g/mg·min ^{1/2})		
Fe ₃ O ₄ @mesoPDA	253.33	24.179	0.831	361.88	2.139	0.930	378.64	0.965	0.977
mesoPDA	260.68	33.449	0.973	354.843	8.244	1			
Fe ₃ O ₄ @PDA	65.80	16.512	0.972	124.36	5.92606	0.963	177.14	2.462	0.958

Table S4 Kinetic parameters of Cr(VI) adsorption onto Fe₃O₄@mesoPDA, mesoPDA, Fe₃O₄@PDA in pH=6.0.

	C_0 (mg/L)	$q_e(\text{exp})$ (mg/g)	Pseudo-first-order model			Pseudo-second-order model		
			k_1 (min ⁻¹)	$q_e(\text{cal})$ (mg/g)	R^2	k_2 (g/mg·min)	$q_e(\text{cal})$ (mg/g)	R^2
Fe ₃ O ₄ @mesoPDA	200	81.19	3.87×10^{-3}	47.78	0.967	3.02×10^{-4}	82.17	0.997
mesoPDA	200	21.24	4.83×10^{-3}	58.1	0.967	2.67×10^{-4}	78	0.997
Fe ₃ O ₄ @PDA	200	76.12	3.75×10^{-3}	17.21	0.934	6.05×10^{-4}	21.84	0.992

	Intraparticle diffusion model								
	C_1	K_1	R_1^2	C_2	K_2	R_2^2	C_3	K_3	R_3^2
	(g/mg·min ^{1/2})			(g/mg·min ^{1/2})			(g/mg·min ^{1/2})		
Fe ₃ O ₄ @mesoPDA	15.46	4.572	0.940	40.22	1.455	0.985	73.11	0.213	1
mesoPDA	3.54	4.558	0.930	32.12	1.632	0.978	71.52	0.121	1
Fe ₃ O ₄ @PDA	0.10	1.233	0.935	6.60	0.502	0.981	18.85	0.063	1

Table S5 Adsorption isotherm parameters of Cr(VI) adsorption onto Fe₃O₄@PDA and mesoPDA in pH=1.5.

Adsorbent	<i>T</i> (K)	Langmuir isotherm			Freundlich isotherm				D-R isotherm			
		<i>q</i> _{max} (mg/g)	<i>b</i> (L/mg)	<i>R</i> ²	<i>R</i> _L	<i>n</i>	<i>K</i> _F (mg/g)	<i>R</i> ²	<i>q</i> ' _{max} (mg/g)	<i>K</i> ' (mol ² /kJ ²)	<i>E</i> (kJ/mol)	<i>R</i> ²
Fe ₃ O ₄ @PDA	298	442.48	0.014	0.988	0.266	5.28	117.88	0.944	452.82	0.0019	16.14	0.994
	308	456.62	0.018	0.989	0.215	6.76	161.58	0.909	507.96	0.0018	16.81	0.895
	318	492.61	0.022	0.991	0.188	7.25	189.125	0.934	565.08	0.0016	17.46	0.904
mesoPDA	298	833.33	0.087	0.997	0.054	6.66	344.58	0.789	965.71	0.0012	20.50	0.958
	308	869.57	0.132	0.997	0.036	13.06	545.1	0.948	989.51	0.00092	23.31	0.935
	318	952.38	0.257	0.996	0.019	14.51	642.466	0.946	1092.46	0.00076	25.64	0.977

Table S6 Comparisons of the Cr(VI) adsorption capacity of different adsorbents.

Adsorbent	pH	Temperatur e (°C)	q_m^a (mg/g)	Kinetics ^b (min)	Ref.
Ethylenediamine-functionalized Fe ₃ O ₄ magnetic polymers	2.5	25	61.35	60	6
Polyaniline-Modified Mg/Al Layered Double Hydroxide Composites	3.0	15	393.70	360	7
CMNP@PDAPs	3.0	30	298.3	200	8
Fe ₃ O ₄ /PPy	2.0	25	209.2	90	9
PPY/ γ -Fe ₂ O ₃	2.0	25	209	15	10
PANI@PS		25	183	~300	11
CS-PDA	2.0	25	374.5	800	12
PEI modified porous SA hydrogel beads	2.0	25	430.88	360	13
CNC@PDA	3.0	15	205	600	14
GA-grafted CS/PEI/Fe ₃ O ₄ composite beads	2.0	25	476.2	600	15
Graphene oxide-dicationic ionic liquid composite	3.0	25	260.92	40	16
ZVI@carbon@polyaniline composite	1.0	25	508	/	17
CMC/CS/PDA@PEI leads	2.0	25	347.0	300	18
Polydopamine microsphere	/	25	180.51	~10	19
Sludge-based magnetic polydopamine Fe ₃ O ₄ @mesoPDA	2.0 1.5	25 25	94.3 574.71	600 <5	20 This work

^a q_m is obtained from the Langmuir isotherm model; ^b Kinetics represents the time of adsorption equilibrium.

Table S7 Thermodynamic parameters of Cr(VI) adsorption onto Fe₃O₄@PDA, mesoPDA, and Fe₃O₄@mesoPDA in pH=1.5.

Adsorbent	<i>T</i> (K)	ΔG^0 (kJ/mol)	ΔH^0 (kJ/mol)	ΔS^0 (kJ/mol·K)	<i>R</i> ²
Fe ₃ O ₄ @PDA	298	-20.004	16.118	0.121	0.999
	308	-21.204			
	318	-22.428			
mesoPDA	298	-24.550	33.831	0.196	0.962
	308	-26.246			
	318	-28.474			
Fe ₃ O ₄ @mesoPDA	298	-23.537	29.937	0.179	0.980
	308	-25.162			
	318	-27.130			

Table S8 The performance comparison of mesoPDA with different scavengers in the Cr(VI) removal in pH=1.5 and pH=6.0.^a

	pH=1.5			pH=6.0			
	No quenching	Ar condition	MeOH pre-extraction	No quenching	Ar condition	MeOH pre-extraction	1 mM BQ
R (%)	100	100	100	38.06	37.94	36.77	41.94
η (%)	/	/	/	/	1.10	3.38	-10.19

^aConditions: pH=1.5, $C_0(\text{VI})=200$ ppm, adsorbent dose=0.5 g/L, $T=298$ K, adsorption time=30 min; pH=6.0, $C_0(\text{VI})=200$ ppm, adsorbent dose =1.0 g/L, $T=298$ K, adsorption time=1440 min; R: Cr(VI) removal rate; η : inhibitory efficiency of scavengers for the Cr(VI) removal.

References

- [1] Y.L. Xu, J.Y. Chen, R. Chen, P.L. Yu, S. Guo and X.F. Wang, *Water Res.*, 2019, 160, 148-157.
- [2] K.Z. Setshedi, M. Bhaumik, S. Songwane, M. S. Onyango and A. Maity, *Chem. Eng. J.*, 2013, 222, 186-197.
- [3] G.B. Kunde, B. Sehgal and A.K. Ganguli, *J. Hazard. Mater.*, 2019, 374, 140-151.
- [4] X.H. Zhu, Y. Xia, X.M. Zhang, A.A. Al-Khalaf, T.C. Zhao, J.X. Xu, L. Peng, W. N. Hozzein, W. Li and D.Y. Zhao, *J. Mater. Chem. A.*, 2019, 7, 8975-8983.
- [5] B.Y. Guan, L. Yu and X.W. Lou, *J. Am. Chem. Soc.*, 2016, 138, 11306-11311.
- [6] Y.G. Zhao, H.Y. Sheng, D. Pan and M.Q. Hu, *J. Hazard. Mater.*, 2010, 182, 295-302.
- [7] K.R. Zhu, Y. Gao, X.L. Tian and C.L. Chen, *ACS Sustain. Chem. Eng.*, 2016, 4, 4361-4369.
- [8] J. Wu, K. Chen, X.L. Tian, M. Fang, X.Y. Hu, Z.W. Tang and X.K. Wang, *Chem. Eng. J.*, 2018, 349, 481-490.
- [9] Y.Q. Wang, B.F. Zhou, T. Gao, X.P. Wu, S.Y. Lou and S.M. Zhou, *J. Mater. Chem.*, 2012, 22, 9034-9040.
- [10] A.E. Chávez-Guajardo, J.C. Medina-Llamas, L. Maqueira, C.A.S. Andrade, K.G.B. Alves and C.P.D. Melo, *Chem. Eng. J.*, 2015, 281, 826-836.

- [11] J. Ding, Y.F. Pan, L.J. Li, H.Z. Liu, Q.X. Zhang, G.D. Gao and B.C. Pan, *Chem. Eng. J.*, 2020, 384, 123232.
- [12] D.M. Guo, Q.D. An, Z.Y. Xiao, S.R. Zhai and D.J. Yang, *Carbohydr. Polym.*, 2018, 202, 306-314.
- [13] Y.Z. Yan, Q.D. An, Z.Y. Xiao, S.R. Zhai, B. Zhai and Z. Shi, *J. Mater. Chem A.*, 2017, 5, 17073-17087.
- [14] L.Q. Dong, R.J. Deng, H.Y. Xiao, F. Chen, Y.F. Zhou, J.K. Li, S. Chen and B. Yan, *Cellulose*, 2019, 26, 6401-6414.
- [15] T. Lu, R.G. Ma, K. Ke, D. Zhang, D.M. Qi and H.T. Zhao, *Chem. Eng. J.*, 2021, 408, 127327.
- [16] J. Shang, Y.N. Guo, D.L. He, W. Qu, Y.N. Tang, L. Zhou and R.L. Zhu, *J. Hazard. Mater.*, 2021, 416, 125706.
- [17] K.D. Gong, Q. Hu, Y.Y. Xiao, X. Cheng, H. Liu, N. Wang, B. Qiu and Z.H. Guo, *J. Mater. Chem A.*, 2018, 6, 11119-11128.
- [18] S.S. Li, X.L. Wang, Q.D. An, Z.Y. Xiao, S.R. Zhai, L. Cui and Z.C. Li, *Int. J. Biol. Macromol.*, 2020, 143, 640-650.
- [19] Q.R. Zhang, Y.X. Li, Q.G. Yang, H. Chen, X.Q. Chen, T.F. Jiao and Q.M. Peng, *J. Hazard. Mater.*, 2018, 342, 732-740.
- [20] C.L. Wan, R. Zhang, L. Wang, X. Liu, D.D. Bao and G.X. Song, *Appl. Surf. Sci.*, 2021, 536, 147980.